Radiative interaction of a focused relativistic electron beam in energy-loss spectroscopy of nanoscopic platelets

M. A. Itskovsky,[1] H. Cohen,[2] and T. Maniv[1]
[1]*Schulich Faculty of Chemistry, Technion-IIT, 32000 Haifa, Israel*
[2]*Chemical Research Support, Weizmann Institute of Science, Rehovot 76100, Israel*
(Received 11 February 2008; revised manuscript received 10 May 2008; published 21 July 2008)

A quantum-mechanical scattering theory for relativistic, highly focused electron beams in the vacuum near nanoscopic platelets is presented, revealing an excitation mechanism due to the electron wave scattering from the platelet edges. Radiative electromagnetic excitations within the light cone are shown to arise, allowed by the breakdown of momentum conservation along the beam axis in the inelastic-scattering process. Calculated for metallic (silver and gold) and insulating (SiO_2 and MgO) nanoplatelets, radiative features are revealed above the main surface-plasmon-polariton peak, and dramatic enhancements in the electron-energy-loss probability at gaps of the "classical" spectra are found. The corresponding radiation should be detectable in the vacuum far-field zone, with e beams exploited as sensitive "tip detectors" of electronically excited nanostructures.

DOI: 10.1103/PhysRevB.78.045419 PACS number(s): 79.20.Uv, 78.67.Bf, 73.20.Mf, 41.60.−m

I. INTRODUCTION

A powerful technique for investigating electromagnetic (EM) field distribution around nanostructures is provided by very fast (relativistic) electron (e) beams, with typical lateral resolution on an atomic scale, available in scanning transmission electron microscopy (STEM).[1–6] As discussed previously, when the e beam is restricted to the vacuum near a selected nanoparticle,[1,2] its EM interaction with surface plasmons or surface-plasmon polaritons (SPPs) (Ref. 7) is reminiscent of the near-field interaction[4] of subwavelength optical probes. Several works have recently studied realizations of Cherenkov radiation excitation within various dielectric media by e beams moving in near-field vacuum zones.[8–11] In all the latter works, the energy-loss processes were described within a simple classical model in which the fast electron is assumed to move with a constant velocity along a straight-line trajectory near a finite dielectric medium such that the energy-loss intensity can be obtained from the force exerted on the electron due to its self-induced electric field through the nearby dielectric medium. The great simplification achieved by this approach amounts to reducing the full scattering problem at hand to a problem of finding the EM field induced by the e beam in the vacuum around the dielectric medium. The resulting EM field can include Cherenkov-type radiative components around the e beam which are restricted, however, to propagation within the interior of the dielectric medium.

In this paper we present a quantum-mechanical theory for the inelastic scattering of a relativistic highly focused e beam traveling near nanoparticles in a "nontouching" aloof configuration.[1,2] We show that the electron wave scattering by nanoparticle edges along the beam axis switches on Cherenkov-type radiation channels which extend into the vacuum away from the nanoparticle. The resulting coupling between the electron and the nanoparticle is found to dramatically enhance various radiative channels in the loss spectrum.

To illustrate our main points, we consider here a simple model (see Fig. 1) where the e beam is propagated in the vacuum along a wide face of a rectangular nanoplatelet (oriented, e.g., in the x-y plane), and a surface or guided wave excited by the electron is propagated with a wave number k_x along the beam axis. The spatially sensitive nature of the corresponding electron-energy-loss process arises from the exponential dependence e^{-2K^*b} of the EM interaction between the e beam and the platelet on the impact parameter b. The extinction coefficient $K^*=\sqrt{K^2-(\omega/c)^2}$, with $K^2=k_x^2+k_y^2$, determines the tail of the evanescent field in the vacuum for values of K outside the light cone, i.e., for $K>\omega/c$. Inside the light cone, i.e., for $K<\omega/c$, K^* is purely imaginary and the corresponding interaction becomes spatially oscillating, allowing the electron to exchange photons with the particle far away into the vacuum. Two mechanisms which can bring K into the light cone are illustrated in Fig. 2, both involving momentum transfer from the e-beam longitudinal motion: (1) to the e-beam transverse motions (by action of the focusing EM lenses) and (2) to the platelet center-of-mass motion (by scattering through the beam-platelet interaction). This striking effect has been overlooked in the recent literature on STEM electron-energy-loss spectroscopy (EELS), since the

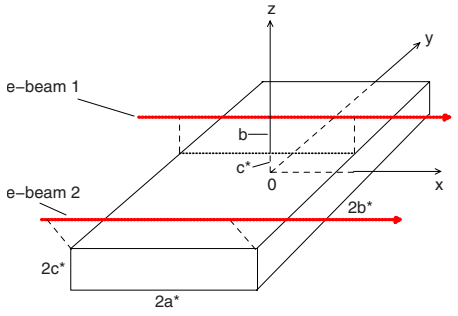

FIG. 1. (Color online) A schematic illustration of the scattering configuration (e beam 1) used in our calculations. a^*,b^*,c^* stand for the platelet half sides along the x,y,z directions, respectively. Another configuration (e beam 2), discussed in Sec. IV in comparison with that in Ref. 12, where the e beam is parallel to an edge of the platelet, is also shown.

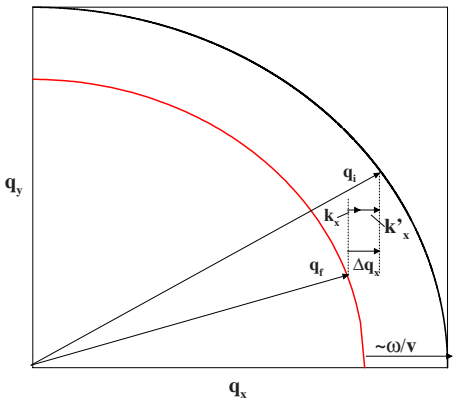

FIG. 2. (Color online) Scattering kinematics which enables platelet excitation wave numbers within the light cone. $\vec{q}_i$ and $\vec{q}_f$ are the initial and final e-beam wave vectors, respectively, and k_x and k_x' are, respectively, the longitudinal wave-vector components of the platelet internal excitation and its recoil.

excitation by an electron moving in the vacuum with a classical velocity v is restricted to a constant longitudinal wave number $k_x=\omega/v>\omega/c$, implying EM coupling to the nanoparticle which is restricted to the evanescent tail near the surface.

Our model calculation is applied to two types of nanoscopic platelets, conducting platelets made of silver or gold and dielectric platelets made of insulators such as silica or magnesia. For both types of nanoparticles, we find significant loss signals in the low-energy range of the spectrum, where the electron-hole excitation probability is either zero (for the insulator) or very small (for the metals), exhibiting far-field (radiative) characteristics. In particular, specific SPP modes of the silver platelet, which penetrate into the light cone, can be excited by the external e beam, leading to features in the EEL spectrum which decay weakly with the beam-platelet distance.

II. MODEL AND FORMULATION

Following Ref. 4, the focused e beam is described here as a one-dimensional wave, propagating along the x axis, while in the transverse (y-z) directions it is described by a wave-packet localized within a smoothly converging cross section along the beam axis, whose shape is assumed to be squared for the sake of simplicity. The corresponding Green's function for the noninteracting focused e beam may be therefore written in the general form

$$G_e^{(0)}(\vec{r},\vec{r}';t)=\frac{1}{2L}\sum_{p_x}e^{iq_x(x-x')}\sum_{\vec{q}_{\rm tr}}e^{i\varepsilon_{p_x,p_{\rm tr}}t/\hbar}\chi_{\vec{q}_{\rm tr}}(y,z;x)\times\chi^*_{\vec{q}_{\rm tr}}(y',z';x'),\tag{1}$$

where $p_x=\hbar q_x$ is the longitudinal (along the beam axis) electron momentum; $\varepsilon_{p_x,p_{\rm tr}}=\sqrt{p_x^2c^2+m_0^2c^4+c^2p_{\rm tr}^2}$ is its total relativistic energy eigenvalue, with m_0 as the electron rest mass; $\vec{p}_{\rm tr}=\hbar\vec{q}_{\rm tr}$ $[\vec{q}_{\rm tr}=(q_y,q_z)]$ is its transverse momentum; and $e^{iq_xx}\chi_{\vec{q}_{\rm tr}}(y,z;x)$ is the corresponding e-beam eigenfunction (see Appendix A).

The EM interaction between the e beam and the platelet may be described effectively by the Hamiltonian

$$\hat{H}_{\rm EM}(\vec{r},\{s\})\approx-e\Phi(\vec{r},\{s\})-e\frac{\hat{p}_x}{mc}A_x(\vec{r},\{s\}),\tag{2}$$

where Φ and A_x are the scalar and x component of the EM four-vector potential, respectively, $\vec{r}$ is the electron position vector, $\{s\}$ is a collective symbol for the position vectors of the platelet charges, and $m=m_0/\sqrt{1-(v/c)^2}$ is the dynamic electron mass.

To first order of the perturbation theory with respect to the EM interaction Hamiltonian $\hat{H}_{\rm EM}$, the probability for the e beam to go, during the time interval τ, from initial to final eigenstates when the platelet initial state is the ground state α_0 is

$$\sum_{\alpha_f}|K^{(1)}_{e(i\to f),\alpha_0\to\alpha_f}(\tau)|^2=\left(\frac{1}{\hbar}\right)^2\sum_{\alpha_f}|\Delta(\varepsilon_{p_x^i,\vec{q}_{\rm tr}^i}+\varepsilon_{\alpha_0},\varepsilon_{p_x^f,\vec{q}_{\rm tr}^f}+\varepsilon_{\alpha_f};\tau)|^2\times\frac{1}{2L}\int_{-L}^{L}dx'\int dy'\int dz'\chi_{\vec{q}_{\rm tr}^f}(y',z';x')\chi^*_{\vec{q}_{\rm tr}^i}(y',z';x')e^{-iq_x^ix'}\langle\alpha_0|\hat{H}_{\rm EM}(\vec{r}')|\alpha_f\rangle e^{iq_x^fx'}\times\frac{1}{2L}\int_{-L}^{L}dx\int dy\int dz\chi^*_{\vec{q}_{\rm tr}^f}(y,z;x)\chi_{\vec{q}_{\rm tr}^i}(y,z;x)e^{-iq_x^fx}\langle\alpha_f|\hat{H}_{\rm EM}(\vec{r})|\alpha_0\rangle e^{iq_x^ix},\tag{3}$$

where the sum is over the platelet final states α_f and $\Delta(\varepsilon,\varepsilon';\tau)\equiv\frac{\exp[i\tau(\varepsilon-\varepsilon')/\hbar]-1}{[i(\varepsilon-\varepsilon')/\hbar]}$.

In the macroscopic time limit $\tau\to\infty$, $|\Delta(\varepsilon,\varepsilon';\tau)|^2\to2\pi\hbar\tau\delta(\varepsilon-\varepsilon')=2\tau\,\mathrm{Re}\int_0^\infty dt\,\exp[it(\varepsilon-\varepsilon')/\hbar]$, and so the rate of change in the scattering probability of the e beam, $R_{e(i\to f)}\equiv\frac{d}{d\tau}\Sigma_{\alpha_f}|K^{(1)}_{e(i\to f),\alpha_0\to\alpha_f}(\tau)|^2$, as $\tau\to\infty$ is given by

$$R_{e(i\to f)} = \frac{4\pi}{\hbar}\sum_{\alpha_f} \mathrm{Re}\Bigg\{ \int_0^\infty dt\, \exp[it(\varepsilon_{p_x^i,\vec{q}_{\mathrm{tr}}^i} + \varepsilon_{\alpha_0} - \varepsilon_{p_x^f,\vec{q}_{\mathrm{tr}}^f} - \varepsilon_{\alpha_f})/\hbar]$$
$$\times \frac{1}{2L}\int_{-L}^{L} dx' \frac{1}{2L}\int_{-L}^{L} dx \int dy' \int dz' \chi_{\vec{q}_{\mathrm{tr}}^f}(y',z';x') \chi^*_{\vec{q}_{\mathrm{tr}}^i}(y',z';x') \int dy \int dz \chi^*_{\vec{q}_{\mathrm{tr}}^f}(y,z;x) \chi_{\vec{q}_{\mathrm{tr}}^i}(y,z;x)$$
$$\times \langle \alpha_0 | e^{-iq_x^i x'} \hat{H}_{\mathrm{EM}}(\vec{r}\,') e^{iq_x^f x'} | \alpha_f \rangle \langle \alpha_f | e^{-iq_x^f x} \hat{H}_{\mathrm{EM}}(\vec{r}) e^{iq_x^i x} | \alpha_0 \rangle \Bigg\}, \tag{4}$$

where the inclusion of all terms under the real part symbol is justified by the reality of the total expression written after the square brackets.

Using the relation $e^{-iq_x^f x}\hat{H}_{\mathrm{EM}}(\vec{r})e^{iq_x^i x} = e^{i(q_x^i - q_x^f)x}\hat{H}^{p_x^f}_{\mathrm{EM}}(\vec{r})$, with $\hat{H}^{p_x^f}_{\mathrm{EM}}(\vec{r}) \equiv (-e)[\hat{\Phi}(\vec{r}) - \frac{p_x^f}{mc}\hat{A}_x(\vec{r})]$, the rate of change in the probability for the scattering of the e beam can be rewritten in the form

$$R_{e(i\to f)} = \sum_{\vec{q}_{\mathrm{tr}}^i, \vec{q}_{\mathrm{tr}}^f} e^{-\beta(\hbar q_{\mathrm{tr}}^i)^2/2m_0} \frac{4\pi}{\hbar} \mathrm{Re}\Bigg[\frac{1}{2L}\int_{-L}^{L} dx' e^{-i\Delta q_x x'} \frac{1}{2L}\int_{-L}^{L} dx e^{i\Delta q_x x} \int dy' \int dz' \chi_{\vec{q}_{\mathrm{tr}}^f}(y',z';x') \chi^*_{\vec{q}_{\mathrm{tr}}^i}(y',z';x')$$
$$\times \int dy \int dz \chi^*_{\vec{q}_{\mathrm{tr}}^f}(y,z;x) \chi_{\vec{q}_{\mathrm{tr}}^i}(y,z;x) \int_0^\infty dt e^{i\omega t} \langle \hat{H}^{p_x^i}_{\mathrm{EM}}(x',y',z';t) \hat{H}^{p_x^f}_{\mathrm{EM}}(x,y,z;0) \rangle \Bigg], \tag{5}$$

where

$$\Delta q_x \equiv (q_x^i - q_x^f) \approx (\omega/v) + \hbar[(q_{tr}^f)^2 - (q_{tr}^i)^2]/2mv \tag{6}$$

is the longitudinal momentum transfer of the e beam (see Appendix A), $\vec{q}_{\mathrm{tr}}^i$ and $\vec{q}_{\mathrm{tr}}^f$ are the e-beam asymptotic transverse momenta, initial and final, respectively, and $\hbar\omega \equiv (\varepsilon_{p_x^i,\vec{q}_{\mathrm{tr}}^i} - \varepsilon_{p_x^f,\vec{q}_{\mathrm{tr}}^i})$ is its energy loss (see Fig. 2). Note that the width β^{-1} of the Gaussian distribution function, is introduced in Eq. (5) to account for the high transverse-energy cutoff caused to the e beam by the objective aperture. It is related to the length L of the region around the beam focal plane used in our model as a normalization factor for the electron wave functions.

The interaction potential $H_{\mathrm{EM}}(x,y,z)$ between the platelet and an external electron at (x,y,z) is nearly independent of x for $|x| \ll a^*$ and decays to zero at least as quickly as $1/x^2$ for $|x| > a^*$ (see, e.g., Ref. 13). Under these circumstances the limits of the integrations over x and x' in the above expression may be set at $-a^*$ and a^*, rather than at $-L$ and L. The correlation function $\langle \hat{H}^{p_x^i}_{\mathrm{EM}}(x',y',z';t)\hat{H}^{p_x^f}_{\mathrm{EM}}(x,y,z;0)\rangle$ can be expressed in terms of the relevant components of the four-tensor photon Green's function $D_{\nu,\mu}(\vec{r}\,',\vec{r};t)$, ν, $\mu = 0,1,2,3$ $(\leftrightarrow ct,x,y,z)$ as

$$\langle \hat{H}^{p_x^i}_{\mathrm{EM}}(x',y',z';t)\hat{H}^{p_x^f}_{\mathrm{EM}}(x,y,z;0)\rangle = i\left[D_{0,0}(\vec{r}\,',\vec{r};t) + \frac{p_x^i}{mc} D_{0,1}(\vec{r}\,',\vec{r};t) + \frac{p_x^f}{mc} D_{1,0}(\vec{r}\,',\vec{r};t) + \frac{p_x^f p_x^i}{(mc)^2} D_{1,1}(\vec{r}\,',\vec{r};t) \right], \quad t > 0. \tag{7}$$

For the sake of simplicity, we may assume translational invariance of the platelet dielectric properties in the x-y plane; that is, take $D_{\nu,\mu}(\vec{r}\,',\vec{r};t) = D_{\nu,\mu}(x-x',y-y',z',z;t)$. For an impact parameter b smaller than the platelet sides along the x and y axes (i.e., $b \ll 2a^*, 2b^*$), this assumption may be justified, though it is inconsistent with the breakdown of momentum conservation in the beam-platelet scattering event considered here (see a more detailed discussion in Sec. III).

Substituting into Eq. (5) for $R_{e(i\to f)}$ and rearranging the integrations, we find that

$$R_{e(i\to f)} = -\frac{4\pi e^2}{\hbar} \sum_{\vec{q}_{\mathrm{tr}}^i, \vec{q}_{\mathrm{tr}}^f} e^{-\beta(\hbar q_{\mathrm{tr}}^i)^2/2m_0} \mathrm{Im}\Bigg[\int dk_x \int dk_y \frac{1}{2L}\int_{-a^*}^{a^*} dx' e^{-i(\Delta q_x - k_x)x'} \int dz' \int dy' e^{ik_y y'} \chi_{\vec{q}_{\mathrm{tr}}^f}(y',z';x') \chi^*_{\vec{q}_{\mathrm{tr}}^i}(y',z';x')$$
$$\times \frac{1}{2L}\int_{-a^*}^{a^*} dx e^{i(\Delta q_x - k_x)x} \int dz \int dy e^{-ik_y y} \chi^*_{\vec{q}_{\mathrm{tr}}^f}(y,z;x) \chi_{\vec{q}_{\mathrm{tr}}^i}(y,z;x) D^{p_x^f, p_x^i}(k_x,k_y,\omega;z',z) \Bigg],$$

where

$$D^{p_x^f,p_x^i}(k_x,k_y,\omega;z',z) = \int_0^\infty dt e^{it\omega} D^{p_x^f,p_x^i}(k_x,k_y;z',z;t),$$

$$D^{p_x^f,p_x^i}(k_x,k_y;z',z;t) = D_{0,0}(k_x,k_y;z',z;t) + \frac{p_x^i}{mc}D_{0,1}(k_x,k_y;z',z;t) + \frac{p_x^f}{mc}D_{1,0}(k_x,k_y;z',z;t) + \frac{p_x^f p_x^i}{(mc)^2}D_{1,1}(k_x,k_y;z',z;t), \tag{8}$$

and $D_{\nu,\mu}(k_x,k_y;z',z;t)$ is the spatial Fourier transform of $D_{\nu,\mu}(x-x',y-y',z',z;t)$ with wave vector $\vec{K}=(k_x,k_y)$.

Now, the four-tensor photon propagator in the vacuum (i.e., at $z,\ z' \leq 0$) has the form[14] (see also Appendix B)

$$D_{\nu,\mu}(k_x,k_y,\omega;z',z) = \frac{\eta_\nu}{2\pi K^*}[\delta_{\nu,\mu}e^{-K^*|z'-z|} - r_{\nu,\mu}(k_x,k_y,\omega)e^{K^*(z'+z)}], \tag{9}$$

in which the relevant part is associated only with the second term within the square brackets (i.e., that associated with the retarded image potential of the e beam). Using this expression and recalling that $1/|K^*|$ is typically much larger than the beam transverse dimension, so that the extreme confinement of the e-beam wave functions $\chi_{\vec{q}_{\rm tr}^{i,f}}$ under the integrals over z and z' restrict their values to a narrow region near $z'=z=-b$, we have

$$R_{e(i\to f)} \approx \frac{4\pi e^2}{\hbar}\sum_{\vec{q}_{\rm tr}^i,\vec{q}_{\rm tr}^f} e^{-\beta(\hbar q_{\rm tr}^i)^2/2m_0}\,{\rm Im}\left[\int dk_x\int dk_y \frac{e^{-2K^*b}}{2\pi K^*}r^{f,i}(k_x,k_y,\omega)\right.$$
$$\left.\times\frac{1}{2L}\int_{-a^*}^{a^*}dx'\,e^{-i(\Delta q_x-k_x)x'}J^*(\vec{q}_{\rm tr}^f,q_{\rm tr}^i;k_y,K^*;x')\frac{1}{2L}\int_{-a^*}^{a^*}dx e^{i(\Delta q_x-k_x)x}J(\vec{q}_{\rm tr}^f,q_{\rm tr}^i;k_y,K^*;x)\right], \tag{10}$$

where

$$r^{f,i}(k_x,k_y,\omega) = r_{0,0}(k_x,k_y,\omega) + \frac{\hbar q_x^i}{mc}r_{0,1}(k_x,k_y,\omega) + \frac{\hbar q_x^f}{mc}r_{1,0}(k_x,k_y,\omega) + \frac{\hbar^2 q_x^f q_x^i}{(mc)^2}r_{1,1}(k_x,k_y,\omega) \tag{11}$$

and

$$J(\vec{q}_{\rm tr}^f,q_{\rm tr}^i;k_y,K^*;x) \equiv \int dz\int dy e^{-ik_y y}\chi^*_{\vec{q}_{\rm tr}^f}(y,z;x)\chi_{q_{\rm tr}^i}(y,z;x). \tag{12}$$

Finally, denoting

$$I(\vec{q}_{\rm tr}^f;\vec{q}_{\rm tr}^i;k_y,K^*;(\Delta q_x-k_x)) \equiv \frac{1}{2L}\int_{-a^*}^{a^*}dx e^{i(\Delta q_x-k_x)x}J(\vec{q}_{\rm tr}^f,q_{\rm tr}^i;k_y,K^*;x), \tag{13}$$

the scattering rate is rewritten as

$$R_{e(i\to f)} = \frac{2e^2}{\hbar}\int dk_x\int dk_y\,{\rm Im}\left[\frac{r^{f,i}(k_x,k_y,\omega)}{K^*}e^{-2K^*b}\right]\sum_{\vec{q}_{\rm tr}^i,\vec{q}_{\rm tr}^f} e^{-\beta(\hbar q_{\rm tr}^i)^2/2m_0}|I(\vec{q}_{\rm tr}^f;\vec{q}_{\rm tr}^i;k_y,K^*;(\Delta q_x-k_x))|^2. \tag{14}$$

In principle, due to the finite size of the platelet, the excitation wave numbers k_x and k_y in Eq. (14) are quantized. Practically, however, for the platelet's lengths of interest (i.e., about 100 nm), additional scattering processes (by structural imperfections, impurities, phonons, and nonideal surfaces) should all smear the corresponding fine mesh ($\Delta k_x \sim \pi/a^* \sim 10^{-3}A^{-1}$) into a continuum.

III. "CLASSICAL" APPROXIMATION AND BEYOND

The theory developed in Sec. II can be further simplified without losing its main physical content by employing several approximations. In the long-wavelength limit discussed in Ref. 14, we find that (see Appendix B)

$${\rm Im}[e^{-2K^*b}r^{f,i}(\vec{k},\omega)/K^*] \approx {\rm Im}\{[(K^\star/k^2)f_e + [(v/c)^2-(\omega/ck)^2]f_o/K^*]e^{-2K^*b}\}, \tag{15}$$

where

$$f_e = (\varepsilon^2 K^{*2}-Q^2)/D_e^+D_e^-, \quad f_o = (K^{*2}-Q^2)/D_o^+D_o^-, \tag{16}$$

$$D_e^+ = \varepsilon K^* + Q\tanh(Qc^*), \quad D_e^- = \varepsilon K^* + Q\coth(Qc^*),$$

$$D_o^+ = K^* + Q\tanh(Qc^*), \quad D_o^- = K^* + Q\coth(Qc^*), \tag{17}$$

$Q=\sqrt{K^2-(\omega/c)^2\varepsilon(\omega)}$, and $\varepsilon(\omega)$ is the local bulk dielectric function of the platelet. In the limit of a semi-infinite medium, the resulting expression reduces (see Appendix B) to the surface dielectric-response function obtained in Ref. 15

by using Maxwell's equations with macroscopic boundary conditions.

The standard classical approximation for the loss function[15] is obtained from Eq. (14) by making the following assumptions: (1) the e-beam transverse momentum distribution function $J(\vec{q}_{\rm tr}^{\,f},\vec{q}_{\rm tr}^{\,i};k_y,K^*;x)=J$ is a constant, that is, equivalent to a δ function in the corresponding real-space transverse coordinates; (2) the contribution of the transverse energy to the longitudinal momentum transfer Δq_x [see Eq. (6)] can be neglected; and (3) the effective particle size a^*, appearing as an integration limit along the beam axis, is infinite. Assumption 3, in conjunction with assumption 1, yields the conservation of longitudinal momentum, i.e., $\Delta q_x - k_x = 0$, which together with assumption 2 imposes the fixed condition $k_x = (\omega/v)$.

It is interesting to note that usually assumption 2 is not strictly satisfied since the contribution of the transverse energy to Δq_x: $\hbar[(q_{\rm tr}^f)^2-(q_{\rm tr}^i)^2]/2mv \approx q_{\rm tr}\Delta q_{\rm tr}/(mv/\hbar) \sim \pm q_{\rm tr}^2/q_x^i$ can be as large in magnitude as ω/v (see Fig. 2). As an example, at $\hbar\omega \sim 10$ eV, $\omega/v \sim 0.05$ nm^{-1}, whereas the transverse-beam–wave-number uncertainty $|\Delta q_{\rm tr}| \sim q_{\rm tr} \sim 2\pi/l$ (with a typical value of $l \sim 0.6$ nm for the beam radius) is 10 nm^{-1}, so that for $\varepsilon_i = 100$ keV, where $q_x^i \sim 1500$ nm^{-1}, $q_{\rm tr}^2/q_x^i \sim 0.07$ nm^{-1}, which is comparable with ω/v.

In the present paper, we focus on the most interesting violation of the "classical" approximation outlined above, allowing a^* to be a finite length, which reflects an effective range of the actual beam-particle interaction along the beam axis. Consequently the longitudinal momentum distribution around $\Delta q_x - k_x = 0$, defined by the integral in Eq. (13), is smeared and many wave numbers k_x inside the light cone start contributing to the loss rate, Eq. (14).

The condition for the smearing to be significant is $\pi/a^* \gtrsim \omega/v$, so that typically for frequencies ω in the visible range, a^* should be smaller than 200 nm. Nanoplatelets of those lengths should dramatically enhance radiative excitations by the e beam, previously overlooked in the literature; see e.g., Ref. 16, where it was argued that recoil effects in STEM should be negligible for valence electron excitations. Recoil is only a classical remnant of the present effect and of less general appearance. In particular, it vanishes for large media, such as the porous film investigated in Ref. 8, for which (if made sufficiently thin) the quantum-mechanical momentum uncertainty along the e-beam axis remains significant.

It should be stressed that, for the sake of simplicity, the platelet dielectric-response function is calculated here by assuming its wide faces to be infinite. Our main conclusions are not expected to change qualitatively by this assumption, however, since the breakdown of translation invariance in the dielectric-response function should further enhance all radiative channels.

Another approximation assumed in the above formalism concerns the cutoff at $x = \pm a^*$ of the integral in Eq. (13). Evidently, the sharp cutoff does not describe properly the smooth attenuation of the e-beam-platelet interaction at $|x|$ values larger than a^*. To improve this approximation, we use in our actual calculations an equivalent Gaussian distribution function, that is,

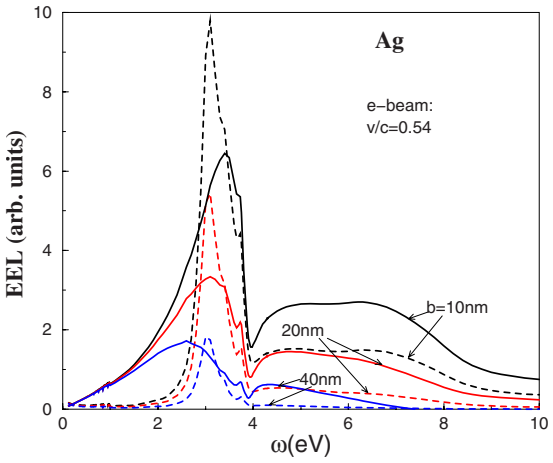

FIG. 3. (Color online) EEL spectra (solid lines) of a 100 keV e beam propagating parallel to the x axis of a rectangular Ag platelet (with half sides $a^*=50$ nm along x and $c^*=10$ nm along z; see Fig. 1) at impact parameters $b=10$, 20, and 40 nm above its wide x-y face. The experimental optical dielectric function $\varepsilon(\omega)$ for silver (Ref. 17) has been exploited. The dashed lines represent spectra calculated by the classical theory.

$$\int_{-a^*}^{a^*} dx e^{i(\Delta q_x - k_x)x} J(\vec{q}_{\rm tr}^{\,f},q_{\rm tr}^i;k_y,K^*;x) \rightarrow J\int_{-\infty}^{\infty} dx e^{i(\Delta q_x - k_x)x} e^{-(x^2/2a^{*2}}. \quad (18)$$

In any event, the exact form of the corresponding distribution function is of no great importance for the main purpose of our present paper.

IV. RESULTS AND DISCUSSIONS

A. Silver and gold nanoplatelets

As a first example, we calculate the EEL function of a 100-nm-long silver and gold platelets for an external 100 keV e beam at various impact parameters (see Figs. 2 and 3). To analyze the various SPP resonances, one may consider the zeros of the denominator of the extraordinary wave amplitude f_e in Eq. (15) in the complex K plane. With the experimental optical dielectric function $\varepsilon(\omega)$, for silver[17] the resulting dispersion relation (Fig. 4) exhibits a rather flat branch of $\omega(\mathrm{Re}\,K)$ inside the light cone, which can be attributed to radiative SPP, seen as a mirror image of the usual nonradiative SP dispersion curve. The sector of $\omega(\mathrm{Re}\,K)$ connecting the two branches across the light line has a vanishing negative slope, where $\mathrm{Im}\,K(\omega) \propto \mathrm{Im}\,\varepsilon(\omega)$ has a sharp peak. The sharp dip in the EEL spectrum just above the classical SP frequency (at 3.8 eV) reflects these closely related features.

At slightly higher frequencies, the EEL signals exhibit a pronounced rise due to the enhanced SPP density of states associated with the flat radiative SPP branch. These peculiar features are missing in the loss spectra of the gold platelet, shown in Fig. 5.

The EEL intensity in this spectral region exhibits attenuation with increasing impact parameter significantly weaker

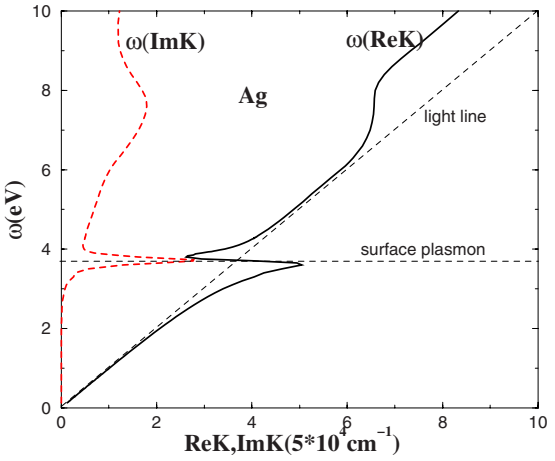

FIG. 4. (Color online) SPP dispersion curves, $\omega(\mathrm{Re}\,K)$ and $\omega(\mathrm{Im}\,K)$, in the complex K plane for silver in the same energy range as in Fig. 3. The experimental optical dielectric function $\varepsilon(\omega)$ for silver (Ref. 17) has been exploited.

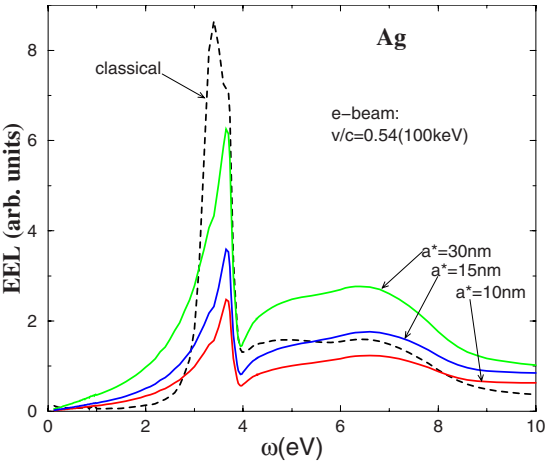

FIG. 6. (Color online) The same as Fig. 3 for three Ag platelets with half sides along the beam axis $a^*=10$, 15, and 30 nm and half width $c^*=15$ nm and with the e beam at an impact parameter $b=10$ nm. The dashed line represents the corresponding classical spectrum (i.e., for $a^*\to\infty$).

than the corresponding attenuation of the main SP peak calculated in the classical limit. The radiative nature of the beam-particle coupling shown in Figs. 3 and 5 is even more pronounced in the low-energy region below the main SP peak, where the classically calculated signal drops to very small values. Here our calculated EEL function exhibits a pronounced broad band with linearly increasing intensity for increasing frequency and almost no attenuation with increasing impact parameter. These features are due to the fact that the loss signal well below the main SP frequency is dominated by the contribution from the ordinary wave amplitude f_o, appearing in Eq. (15), which is singularly enhanced near the light line (where $K^*\to 0$), and thus reflecting the nearly pure (transverse) photonic nature of the excitations by the e beam in this "classically forbidden" region.

The results of our calculations may be compared to the experimental data reported in Ref. 18 for silver and gold nanorods and ellipsoids. Figure 6 shows our calculated EEL spectra for three silver platelets with $c^*=15$ nm and $a^*=10$, 15, and 30 nm at impact parameter $b=10$ nm. The shown curves may be compared to the spectrum in Ref. 18 obtained for a silver ellipsoid with a long half axis (~ 30 nm) and two short half axes (~ 15 nm) at impact parameter ~ 10 nm above the ellipsoid wide face.

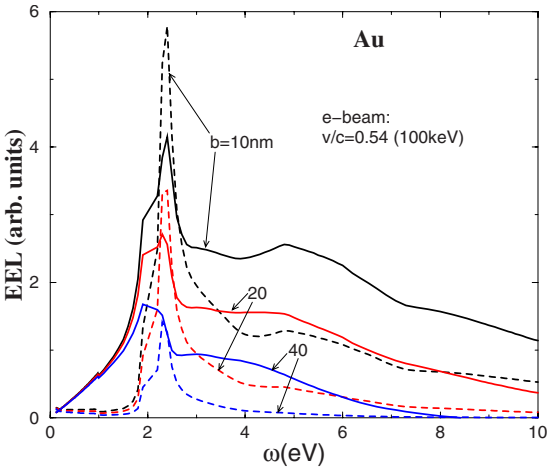

FIG. 5. (Color online) The same as Fig. 3 for a platelet made of gold (Au). Note the absence of the sharp dips appearing just above the main plasmon peaks in the corresponding Ag spectra (Fig. 3).

The two lower curves, particularly those corresponding to $a^*=10$ nm, exhibit good agreement with the relevant experimental data. Specifically, in addition to the very good agreement of the calculated main plasmon peak position ($\simeq 3.45$ eV) with the experimental one, the ratio (~ 2) of the intensity of the main plasmon peak to that of the high-energy broad peak and the extent and magnitude of the low-energy tail shown in Fig. 6 are seen to agree pretty well with the corresponding experimental results. In contrast a large intensity ratio (~ 8) and a very small low-energy tail characterize the classical curve shown in Fig. 6, both indicating the importance of the quantum effects predicted by our theory. Note that an important feature of our calculated spectra, the large dip just above the main plasmon peak, which is missing in the experimental data, is shown to develop only at relatively large values of a^* (i.e., for $a^*>20$ nm).

B. Insulating nanoplatelets

The situation in the forbidden energy-gap region of semiconductors and insulators is in a sense an extreme case of the effect demonstrated in the low-energy region in Fig. 3: The EEL spectra shown in Fig. 7 are calculated for an external 100 keV e beam, propagating parallel to the x-y face of a 100-nm-long SiO_2 platelet with half thickness $c^*=50$ nm, at different impact parameters b. The spectra reveal a pronounced double-peak structure within the forbidden gap region, which does not decay with increasing b values. Strictly speaking, this structure reduces to a single broad peak for platelets of widths $c^*\lesssim 10$ nm, reflecting a finite-size effect. Similarly to the situation with the silver and gold platelets well below the main SP peak, the strong radiative nature of

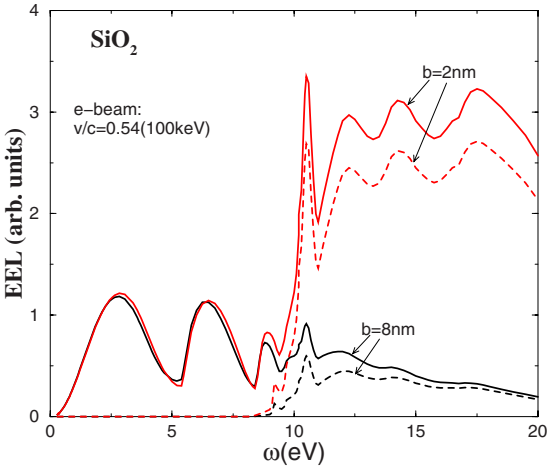

FIG. 7. (Color online) EEL spectra (solid lines) of a 100 keV e beam propagating parallel to the x axis of a rectangular SiO_2 platelet at distances $b=2$ and 8 nm above its wide (x-y) face. The platelet half sides along the x and z axes are $a^*=50$ nm and $c^*=50$ nm, respectively. Note the finite-size oscillations of the calculated loss signal inside the forbidden energy gap with a period roughly proportional to $1/c^*$. The corresponding spectra (dashed lines) obtained from the classical theory are also shown for comparison. Note the close similarity of the classical spectrum for $b=8$ nm with the one obtained in Ref. 12 for the same e-beam velocity at nearly the same impact parameter parallel to a sharp wedge (see Fig. 1).

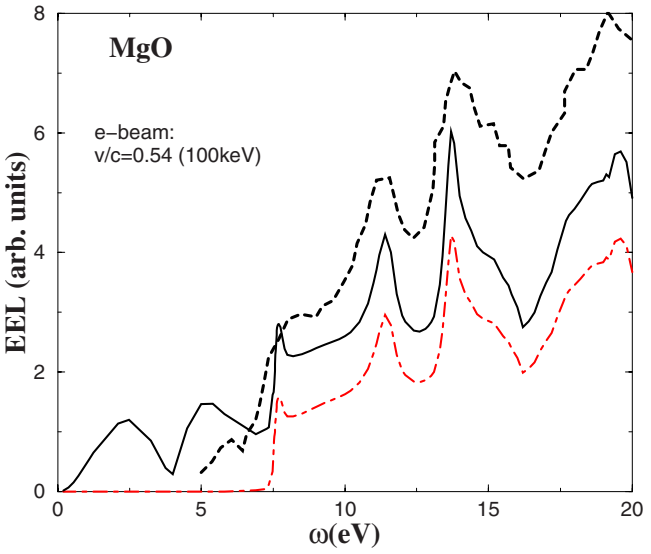

FIG. 8. (Color online) Calculated EEL spectrum (solid line) of a 100 keV e beam propagating parallel to the x axis of a rectangular MgO platelet at a distance $b=2$ nm above its wide (x-y) faces. The platelet half sides along the x and z axes are $a^*=50$ nm and $c^*=50$ nm, respectively. The corresponding classical ($a^*\to\infty$) result (dotted-dashed line) is also shown. The dashed line shows the experimental data reported in Ref. 19 for a MgO smoke cube of 100 nm size, with a normalization factor determined by equating the measured EEL signal to the calculated one at $\omega=7.5$ eV.

this feature arises from the ordinary wave amplitude f_o, corresponding to the excitation of purely transverse EM waves, polarized within the x-y plane, which totally dominates the loss signal in the forbidden gap region. The spectra shown in Fig. 7 may be compared to the results reported in Ref. 12 for an electron moving parallel to a 90° SiO_2 wedge at a distance of 8.5 nm (see Fig. 1). The pronounced radiative broad band within the gap region, obtained in our calculation, dramatically contrasts the vanishing loss signal shown in Fig. 4 for an electron beam with the same velocity ($v=0.54c$) and nearly the same impact parameter. The lack of far-field (radiative) coupling between the external e beam and the dielectric medium in the latter theoretical approach restricted the fast beam to excitation, through near-field coupling, of EM waves confined within the dielectric medium,[8] similar to ordinary waveguide modes which can develop within a thin SiO_2 slab in the forbidden gap region, where Re $\varepsilon(\omega)\approx 2$ and Im $\varepsilon(\omega)\to 0$. For an ideal planar geometry (as assumed in our calculation of the dielectric-response function $r(\vec{K},\omega)$, the corresponding waveguide modes appear as extremely narrow resonances which cannot be excited by an e beam with Δq_x values outside the light cone due to the vanishingly small dielectric damping, Im $\varepsilon(\omega)$.

Such radiation excitations become possible for the nonplanar geometries studied in Refs. 8 and 12 even under the rigid e-beam trajectory approximation exploited there (but only above a threshold beam energy considerably higher than 100 keV) due to the translational symmetry-broken dielectric media considered in their calculations. Yet, the corresponding Cherenkov-type channels remain fundamentally different from the ones we propose: The opening of scattering channels with wave numbers inside the light cone allows coupling of the e beam to the *continuum* of EM modes which are extended into the vacuum perpendicular to the platelet wide face. The relative strength of the present radiative mechanism may be further appreciated by noting the calculated spectra near the sharp SiO_2 wedge in Ref. 12, where in spite of the geometrical enhancement of near-field Cherenkov coupling, beam energies far above 100 keV were needed there for "switching on" such channels.

Finally, it is instructive to compare our predicted loss spectrum of an external 100 keV e beam propagating near a MgO platelet with half sides $a^*=c^*=50$ nm at an impact parameter $b=2$ nm (see Fig. 8) to the experimental data reported in Ref. 19 for a MgO smoke cube of 100 nm size. The overall agreement is good, including the occurrence, in both the calculated spectrum and the experimental data, of a broad, nonvanishing signal within the forbidden gap region, which is missing in the classically calculated spectrum. In this gap region, the calculated spectrum exhibits a structure associated with the multiple reflection of the generated radiation between the two parallel faces of the platelet perpendicular to the z axis. This finite-size effect is peculiar to the far-field radiative modes found in the present paper for platelets confined in the direction along the e-beam axis and is different from (though related to) the extremely sharp resonances associated with the waveguide modes developed in an "ideal" (i.e., wide laterally) planar dielectric thin film. The classical approach applied to such an ideal film yields usually (i.e., except for extremely rare coincidences of the loss energy with the resonant frequencies) null loss intensity, whereas in our quantum calculations the continuous window of wave numbers inside the light cone removes the stringent

resonant conditions and allows the appearance of a significant loss intensity in the entire gap region.

Quantitatively, the agreement between the experimental MgO data and our calculated spectrum in the sub-band gap region is limited. This may partially arise from inaccuracies in the subtraction of the experimental elastic tail and also from the sensitivity of the calculated data to smearing effects acting on the nominally quantized excitation wave number. Application of monochromated EELS to the MgO system may be helpful in studying this discrepancy.

V. CONCLUSION

Applying a quantum-mechanical approach to the scattering problem of highly focused relativistic e beams near nanoplatelets, we have shown that Cherenkov-type radiation of STEM e beams, discussed recently in the literature,[8–10] has a much broader scope than originally presented. Dramatic enhancements of radiative channels arise from the breakdown of momentum conservation along the e-beam axis in the inelastic process due to scattering of the electron wave by the nanoparticle edges. Further enhancements, realized due to the extreme lateral confinement of the e beam and its associated transverse momentum uncertainty,[4] have not been considered in detail here. The radiation predicted to be emitted from both conducting and insulating nanoplatelets can be generated at impact parameters larger than the evanescent tail of the excited surface EM modes due to the oscillatory distance dependence of the electron-platelet interaction for momentum transfers within the light cone. Consequently, this radiation should have a significant propagation component perpendicular to its main direction along the e-beam axis.

Large deviations from the classical EEL signal, due to radiative interaction, are found to exist also at relatively small impact parameters, which can be readily tested experimentally. Their nature as arising from radiative interaction may be confirmed experimentally by varying the impact parameter in a relatively small range due the strong (exponential) attenuation of the EEL signal associated with near-field interaction at impact parameters in the range of 10 nm or so. The signal surviving this sharp attenuation (i.e., at subwavelength distances) is dominated by radiative interaction.

The results of our calculations for silver platelets seem to agree pretty well with the experimental data reported in Ref. 18 for silver nanoellipsoids. Furthermore, experimental observation of loss signals within the forbidden energy gap of MgO cubes of 100 nm size by Aizpurua *et al.*[19] seems as well to support our main prediction. Application of the theoretical framework used here to additional scattering and nanoparticle configurations will enable detailed examination of the predicted effects and interesting applications of the focused beam spectroscopy in nanostructured arrays. Experimental confirmation of the predicted radiative interaction may lead to applications of fast, highly focused e beams as sensitive tip detectors of radiation field around electronically excited nanostructures.

ACKNOWLEDGMENTS

We thank Boris Lembrikov for helpful discussions. This research was supported by Argentinian Research Fund and by the fund for the promotion of research at the Technion.

APPENDIX A

In this appendix we specialize our general model of the focused e beam to allow a more detailed discussion of some aspects of EELS experiments in STEM pertinent to the subject under study in this paper. We employ the relativistic Schrödinger's wave equation,

$$\left[-\left(\frac{\partial^2}{\partial y^2}+\frac{\partial^2}{\partial z^2}\right)-\frac{\partial^2}{\partial x^2}\right]\psi(x,y,z)=\tilde{\varepsilon}^2\psi(x,y,z),$$

$$\tilde{\varepsilon}^2\equiv\varepsilon^2/\hbar^2c^2-m_0^2c^2/\hbar^2,$$

subject to the boundary conditions

$$\begin{aligned}&\psi(x,y,z)=0, \quad \text{for} \quad l(x)\geq y\geq 0\\ &\qquad\qquad \text{and,} \quad \text{for} \quad l(x)-b\geq z\geq -b,\\ &\qquad\qquad \text{with} \quad l(x)=l_0+\alpha|x|, \quad \alpha\ll 1.\end{aligned} \tag{A1}$$

Due to the small converging angle α, one may invoke the Born-Oppenheimer approximation, $\psi(x,y,z)=\varphi(x)\chi(y,z;x)$, in which the crossed derivatives $\frac{\partial}{\partial x}\chi(y,z;x)$, $\frac{\partial^2}{\partial x^2}\chi(y,z;x)$ are neglected, and the wave equation takes the approximate form

$$-\frac{1}{\chi(y,z;x)}\left(\frac{\partial^2}{\partial y^2}+\frac{\partial^2}{\partial z^2}\right)\chi(y,z;x)-\frac{1}{\varphi(x)}\frac{\partial^2}{\partial x^2}\varphi(x)=\tilde{\varepsilon}^2$$

subject to the boundary conditions, Eq. (A1). Solutions for the "slow" motion wave equation satisfying these boundary conditions are $\chi_{n_y,n_z}(y,z;x)=\frac{1}{l(x)}\sin\{q_y(x)[y-l(x)]\}\sin\{q_z(x)[z+b-l(x)]\}$, where $q_{y,z}(x)=\pi n_{y,z}/l(x)$, with $n_{y,z}=1,2,\ldots$. The resulting equation for the "fast" motion is

$$\left[-\frac{d^2}{dx^2}+v_n^2(x)\right]\varphi(x)=\tilde{\varepsilon}^2\varphi(x), \tag{A2}$$

where $v_n^2(x)=q_y^2(x)+q_z^2(x)$.

Thus, to first order in perturbation theory with respect to $v_n^2(x)$, the energy eigenvalues of an electron "trapped" by the EM lenses inside the conic beam region are given by

$$\varepsilon_{p_x,n}^2=\hbar^2c^2\tilde{\varepsilon}^2+m_0^2c^4\approx p_x^2c^2+m_0^2c^4+c^2\hbar^2(\pi n/l)^2,$$

$$n^2=n_y^2+n_z^2, \tag{A3}$$

where $p_x=\hbar q_x$ is the e beam main (longitudinal) momentum and $p_{y,z}=\hbar\pi n_{y,z}/l$, with $n_{y,z}=1,2,\ldots,l=\sqrt{l_0(l_0+\alpha L)}$, its transverse momentum components in the free propagation zone outside the EM focusing domain.

This model of the e beam is, of course, a drastic simplification of the actual focused beam in STEM. In particular the ideally reflecting boundary conditions, Eq. (A1), cannot be strictly realized under the smoothly varying field generated in space by the focusing EM lenses. The results of our analysis here are not expected to be very sensitive to the fine details of the momentum distribution of the beam. We may take advantage of that by eliminating the specific depen-

dence of the transverse wave numbers on the average beam radius l and replace $(\pi/l)(n_y,n_z)$ with the general symbol $\vec{q}_{\rm tr}$, such that the specialized set of eigenfunctions, $\chi_{n_y,n_z}(y,z;x)$, may be replaced by a more general set $\chi_{\vec{q}_{\rm tr}}(y,z;x)$.

The relativistic asymptotic (initial and final) energies of an electron trapped within the beam double-cone boundary are $\varepsilon_{i,f}^2=m_0^2c^4+(p_x^2c^2+\frac{\hbar^2\pi^2n^2c^2}{l^2})_{i,f}=[m_0^2c^4+(p_x^{i,f})^2c^2]+[(p_y^{i,f})^2+(p_z^{i,f})^2]c^2$, where $(p_x^{i,f})^2=(\varepsilon_{i,f}^2-m_0^2c^4)/c^2-[(p_y^{i,f})^2+(p_z^{i,f})^2]$. The corresponding longitudinal momentum transfer is calculated from

$$(q_x^i-q_x^f)(q_x^i+q_x^f)=(\varepsilon_i-\varepsilon_f)(\varepsilon_i+\varepsilon_f)/(\hbar c)^2+[(q_{\rm tr}^f)^2-(q_{\rm tr}^i)^2],$$

where

$$(q_x^i+q_x^f)\approx 2mv/\hbar,\quad (\varepsilon_i+\varepsilon_f)\approx(2mc^2),$$

so that

$$(q_x^i-q_x^f)2mv/\hbar\approx(\varepsilon_i-\varepsilon_f)(2mc^2)/(\hbar c)^2+[(q_{\rm tr}^f)^2-(q_{\rm tr}^i)^2],$$

namely,

$$\Delta q_x\approx(\omega/v)+\hbar[(q_{\rm tr}^f)^2-(q_{\rm tr}^i)^2]/2mv.$$

APPENDIX B

In this appendix, following the method developed in Ref. 14, we consider the dielectric loss function $\mathrm{Im}[\frac{r^{f,i}(k_x,k_y,\omega)}{K^*}e^{-2K^*b}]$ appearing in Eq. (14) and show that it is proportional to $\mathrm{Re}\,E_x(\vec{K};-b;\omega)$—the electric-field component along the e beam axis at the beam position $z=-b$. The latter is the key ingredient in the calculation of the power loss function in the classical limit. We shall also show in this appendix that in the long-wavelength limit discussed in Ref. 14, the dielectric loss function reduces to the well known expression derived in Ref. 15.

Our analysis starts from the expectation value of the four-vector potential $[A_\nu=(\varphi,-\vec{A})]$, given by

$$A_\nu(\vec{r},t)=\frac{1}{c}\sum_{\mu=0}^{3}\int_{-\infty}^{\infty}dt'\int d^3r'D_{\nu,\mu}(\vec{r},\vec{r}';t-t')j^{{\rm ext},\mu}(\vec{r}',t'),\tag{B1}$$

where $j^{{\rm ext},\mu}(\vec{r}',t')$ is the external four-current density generated by the e beam [with the components $j^{{\rm ext},\nu}=(c\rho^{\rm ext},\vec{j}^{\rm ext})$], and $D_{\nu,\mu}(\vec{r},\vec{r}';t-t')$ is the "dressed" retarded photon Green's function, defined by the correlator

$$D_{\nu,\mu}(\vec{r},\vec{r}';t-t')=-i\langle[\hat{A}_\nu(\vec{r},t),\ \hat{A}_\mu(\vec{r}',t')]\rangle\theta(t-t').\tag{B2}$$

The "bare" four-vector potential is given by

$$A_\nu^{(0)}(\vec{r},t)=\frac{1}{c}\int_{-\infty}^{\infty}dt'\int d^3r'D_\nu^{(0)}(\vec{r}-\vec{r}';t-t')j^{{\rm ext},\nu}(\vec{r}',t'),$$

where $D_{\nu,\mu}^{(0)}(\vec{r},\vec{r}';t-t')\equiv D_\nu^{(0)}(\vec{r}-\vec{r}';t-t')\delta_{\nu,\mu}$, is the bare retarded photon propagator in the Lorentz gauge, which is given by $D_\nu^{(0)}(\vec{r}-\vec{r}';t-t')=\eta_\nu\theta(t-t')\delta(|\vec{r}-\vec{r}'|/c+t-t')/|\vec{r}-\vec{r}'|$, with

$$\eta_\nu=\begin{pmatrix}1, & \nu=0\\ -1, & \nu=1,2,3\end{pmatrix}.$$

The corresponding Fourier transforms with respect to the spatial coordinates parallel to the surface, with wave vector $\vec{K}=(k_x,k_y)$, are

$$A_\nu(\vec{K};z;\omega)=\frac{1}{c}\sum_{\mu=0}^{3}\int dz'D_{\nu,\mu}(\vec{K};z,z';\omega)j^{{\rm ext},\mu}(\vec{K};z';\omega),$$

and

$$D_\nu^{(0)}(\vec{K},z,z';\omega)=D_\nu^{(0)}(K^*,|z-z'|)=\frac{\eta_\nu}{2\pi K^*}e^{-K^*|z-z'|}.$$

Our explicit expression for the external four-current density associated with the e beam is

$$j^{{\rm ext},\mu}(\vec{K};z';\omega)=\begin{cases}-ce\delta(z+b)\delta(vk_x-\omega), & \mu=0\\ -e\left(\dfrac{\omega}{k_x}\right)\delta(z+b)\delta(vk_x-\omega), & \mu=1\\ 0, & \mu=2,3.\end{cases}\tag{B3}$$

For $z,z'\le 0$, i.e., both on the vacuum side of the dielectric slab, occupying the space $2c^*>z>0$, the lateral Fourier transform of Eq. (B2) can be written in the form

$$D_{\nu,\mu}(\vec{K},z,z';\omega)=\frac{\eta_\nu}{2\pi K^*}\begin{bmatrix}\delta_{\nu,\mu}e^{-K^*|z-z'|}\\ -(r_{\nu,\mu}^{(\rm odd)}+r_{\nu,\mu}^{(\rm even)})e^{K^*(z+z')}\end{bmatrix},\tag{B4}$$

where the generalized reflection four matrices for incident waves, which are either symmetric or antisymmetric with respect to the slab center, are given respectively by (see Ref. 14)

$$\mathbf{r}^{(\rm odd,even)}=\frac{1}{2}(\mathbf{W}^{(\rm odd,even)}-\mathbf{I}),$$

$$\mathbf{W}^{(\rm odd,even)}\equiv(\mathbf{U}^{(\rm odd,even)}+I)^{-1}.\tag{B5}$$

(The definition of the matrix $\mathbf{U}$ can be found in Ref. 14.)

In the limit of a semi-infinite slab $(c^*\to\infty)$, $\mathbf{r}^{(\rm odd)}=\mathbf{r}^{(\rm even)}\equiv\mathbf{r}$, so that

$$r_{\nu,\mu}^{(\rm odd)}+r_{\nu,\mu}^{(\rm even)}\to 2r_{\nu,\mu},\quad c^*\to\infty$$

and

$$A_\nu(\vec{K};z;\omega)=-\frac{1}{c}\frac{\eta_\nu}{2\pi K^*}(\delta_{\nu,0}e^{-K^*|z+b|}-2r_{\nu,0}e^{K^*(z-b)})\times ce\delta(vk_x-\omega)-\frac{1}{c}\frac{\eta_\nu}{2\pi K^*}(\delta_{\nu,1}e^{-K^*|z+b|}-2r_{\nu,1}e^{K^*(z-b)})e\left(\frac{\omega}{k_x}\right)\delta(vk_x-\omega),$$

where at $z=-b$

$$A_\nu(\vec{K};-b;\omega) = -\frac{e}{2\pi K^*}\delta(vk_x-\omega)\eta_\nu\left\{\left[\delta_{\nu,0}+\left(\frac{\omega}{ck_x}\right)\delta_{\nu,1}\right] - \left[2r_{\nu,0}+\left(\frac{\omega}{ck_x}\right)2r_{\nu,1}\right]e^{-2K^*b}\right\}. \quad \text{(B6)}$$

To simplify the calculation, we shall consider in what follows the special case where the wave vector $\vec{K}$ is parallel to the e-beam direction, which was selected along the x axis, so that $k_y=0$, and $K=k_x$. Thus, the electric-field component along the e-beam axis at the beam position $z=-b$, $E_x(\vec{K};-b;\omega)$, can be calculated from the explicit expressions for the potentials in Lorentz gauge, namely,

$$\begin{aligned}E_x(\vec{K};-b;\omega) &= -ik_xA_0(\vec{K};-b;\omega)-i(\omega/c)A_1(\vec{K};-b;\omega)\\ &= \left[-ik_x\left[r_{0,0}+\left(\frac{\omega}{ck_x}\right)r_{0,1}\right]\right.\\ &\quad \left.-i(\omega/c)\left[r_{1,0}+\left(\frac{\omega}{ck_x}\right)r_{1,1}\right]\right]e^{-2K^*b}\\ &= -ik_x\left[r_{0,0}+\left(\frac{\omega}{ck_x}\right)r_{0,1}+\left(\frac{\omega}{ck_x}\right)r_{1,0}\right.\\ &\quad \left.+\left(\frac{\omega}{ck_x}\right)^2r_{1,1}\right]e^{-2K^*b},\end{aligned}$$

or (by exploiting the symmetry property $r_{1,0}=-r_{0,1}$,[14]

$$E_x(\vec{K};-b;\omega) = -ik_x\left[r_{0,0}+\left(\frac{\omega}{ck_x}\right)^2r_{1,1}\right]e^{-2K^*b}. \quad \text{(B7)}$$

This expression should be compared to the dielectric-response function

$$\begin{aligned}r^{f,i}(k_x,k_y,\omega) &= r_{0,0}+(\hbar q_x^i/mc)r_{0,1}+(\hbar q_x^f/mc)r_{1,0}\\ &\quad +[\hbar^2q_x^fq_x^i/(mc)^2]r_{1,1},\end{aligned}$$

which may be simplified (again due to the symmetry $r_{1,0}=-r_{0,1}$ and the inequality $|\Delta q_x|\approx\omega/v\ll mc/\hbar$) to

$$\begin{aligned}r^{f,i}(k_x,k_y,\omega) &= r_{0,0}+(v/c)^2r_{1,1}+(\hbar\Delta q_x/mc)[r_{0,1}-(v/c)r_{1,1}]\\ &\approx r_{0,0}+(v/c)^2r_{1,1}+(\hbar\omega/mcv)[r_{0,1}-(v/c)r_{1,1}]\\ &\approx r_{0,0}+(v/c)^2r_{1,1}. \quad \text{(B8)}\end{aligned}$$

Thus, since in the classical limit the prefactor of $r_{1,1}$ in Eq. (B7) $(\frac{\omega}{ck_x})^2 \leftarrow\rightarrow (v/c)^2$, we find that

$$\text{Re}\, E_x(\vec{K};-b;\omega) \propto \text{Im}[[r_{0,0}+(v/c)^2r_{1,1}]e^{-2K^*b}].$$

Exploiting the continuity equation to connect various components of the matrix $\mathbf{U}$,[14]

$k_xU_{11}-(\omega/c)U_{01}=-K^*U_{31}$ and $k_xU_{13}-(\omega/c)U_{03}=-K^*U_{33}$, and noting the symmetry relation $U_{31}=-U_{13}$, it can be shown that

$$r_{0,0}+\left(\frac{\omega}{ck_x}\right)r_{0,1} = -\frac{(\omega/ck_x)U_{01}+U_{00}}{2(1+\text{Tr}\,\mathbf{U})}.$$

Furthermore, the continuity equation also implies

$$k_xU_{01}+(\omega/c)U_{00}=K^*U_{30} \text{ and } k_xU_{13}-(\omega/c)U_{03}=-K^*U_{33},$$

so that since $U_{30}=U_{03}$, we also find that

$$r_{1,0}+\left(\frac{\omega}{ck_x}\right)r_{1,1} = \frac{U_{01}-(\omega/ck_x)U_{11}}{2(1+\text{Tr}\,\mathbf{U})}.$$

Consequently $r_{0,0}+(v/c)^2r_{1,1}\rightarrow r_{0,0}+(\frac{\omega}{ck_x})^2r_{1,1}$ $=-\frac{U_{00}+(\omega/ck_x)^2U_{11}}{2(1+\text{Tr}\,\mathbf{U})}$ and in the long-wavelength limit, where $1+\text{Tr}\,\mathbf{U}=\frac{(\varepsilon K^*+Q)}{2\varepsilon K^*}$ and ε is the bulk optical (frequency dependent) dielectric function of the platelet, we find

$$U_{0,0} = \frac{(1-\varepsilon)}{2\varepsilon}\left[1+\frac{(\omega/c)^2}{2K^{*2}}\right], \quad \text{(B9)}$$

$$U_{1,1} = \frac{(\varepsilon-1)}{\varepsilon}\frac{(\omega/c)^2}{4K^{*2}}\left[1+(\varepsilon-1)\frac{K^{*2}}{(Q+K^*)^2}\right], \quad \text{(B10)}$$

so that finally

$$\text{Re}\, E_x(\vec{K};-b;\omega) \propto \text{Im}\left\{\frac{e^{-2K^*b}}{K^*}\left[\frac{K^*(\varepsilon-1)}{(\varepsilon K^*+Q)}+\left(\frac{v}{c}\right)^2 \times\left(\frac{(K^*-Q)}{(Q+K^*)}+\frac{(1-\varepsilon)K^2}{(Q+K^*)(\varepsilon K^*+Q)}\right)\right]\right\},$$

which is equivalent to surface dielectric loss function obtained in Ref. 15 by using Maxwell's equations with macroscopic boundary conditions.

[1] P. E. Batson, Ultramicroscopy **11**, 299 (1983).
[2] A. Howie and R. H. Milne, Ultramicroscopy **18**, 427 (1985); P. M. Echenique and A. Howie, *ibid.* **16**, 269 (1985).
[3] D. A. Muller, W. Tsou, R. Raj, and J. Silcox, Nature (London) **366**, 725 (1993).
[4] H. Cohen, T. Maniv, R. Tenne, Y. Rosenfeld Hacohen, O. Stephan, and C. Colliex, Phys. Rev. Lett. **80**, 782 (1998); P. M. Echenique, A. Howie, and R. H. Ritchie, *ibid.* **83**, 658 (1999); H. Cohen, T. Maniv, R. Tenne, Y. Rosenfeld Hacohen, O. Stephan, and C. Colliex, *ibid.* **83**, 659 (1999).
[5] B. I. Lembrikov, M. A. Itskovsky, H. Cohen, and T. Maniv, Phys. Rev. B **67**, 085401 (2003).
[6] H. Cohen, B. I. Lembrikov, M. A. Itskovsky, and T. Maniv, Nano Lett. **3**, 203 (2003).
[7] H. Raether, *Excitation of Plasmons and Interband Transitions by Electrons* (Springer, New York, 1980).
[8] N. Zabala, A. G. Pattantyus-Abraham, A. Rivacoba, F. J. Garcia de Abajo, and M. O. Wolf, Phys. Rev. B **68**, 245407 (2003).
[9] F. J. Garcia de Abajo and A. Howie, Phys. Rev. Lett. **80**, 5180 (1998); F. J. Garcia de Abajo, Phys. Rev. B **59**, 3095 (1999).
[10] Tetsuyuki Ochiai and Kazuo Ohtaka, Phys. Rev. B **69**, 125106 (2004).

[11] F. J. Garcia de Abajo, N. Zabala, A. Rivacoba, A. G. Pattantyus-Abraham, M. O. Wolf, and P. M. Echenique, Phys. Rev. Lett. **91**, 143902 (2003).
[12] F. J. Garcia de Abajo and A. Howie, Phys. Rev. B **65**, 115418 (2002).
[13] T. L. Ferrell, R. J. Warmack, V. E. Anderson, and P. M. Echenique, Phys. Rev. B **35**, 7365 (1987).
[14] T. Maniv and H. Metiu, J. Chem. Phys. **76**, 696 (1982); T. Maniv, Phys. Rev. B **26**, 2856 (1982).
[15] Z. I. Wang, Micron **27**, 265 (1996).
[16] R. H. Ritchie and A. Howie, Philos. Mag. A **58**, 753 (1988).
[17] *Handbook of Optical Constants of Solids II*, edited by Edward D. Palik (Academic, Boston, 1991).
[18] M. Bosman, V. J. Keast, M. Watanabe, A. I. Maaroof, and M. B. Cortie, Nanotechnology **18**, 165505 (2007).
[19] J. Aizpurua, B. Rafferaty F. J. Garcia de Abajo, and A. Howie, Inst. Phys. Conf. Ser. **8**, 277 (1997).